



# Well-resolved variations in the formation ages for Ca–Al-rich inclusions in the early Solar System

G.J. MacPherson<sup>a,\*</sup>, N.T. Kita<sup>b</sup>, T. Ushikubo<sup>b</sup>, E.S. Bullock<sup>a</sup>, A.M. Davis<sup>c,d</sup>

<sup>a</sup> Department of Mineral Sciences, National Museum of Natural History, Smithsonian Institution, Washington, DC 20560, United States

<sup>b</sup> WiscSIMS, Department of Geoscience, University of Wisconsin–Madison, Madison, WI 53706, United States

<sup>c</sup> Department of the Geophysical Sciences, University of Chicago, Chicago, IL 60637, United States

<sup>d</sup> Enrico Fermi Institute, University of Chicago, Chicago, IL 60637, United States

## ARTICLE INFO

### Article history:

Received 14 September 2011

Received in revised form 23 February 2012

Accepted 3 March 2012

Available online xxxx

Editor: B. Marty

### Keywords:

<sup>26</sup>Al

calcium–aluminum-rich inclusions

chronology

early Solar System

## ABSTRACT

Recent whole-rock magnesium-isotopic data for calcium-aluminum-rich inclusions (CAIs) in chondrite meteorites indicate that the primary nebular fractionation of aluminum from magnesium, probably by condensation, occurred within <20,000 years at 4.567 Ga. However, high-precision multicollector ion microprobe data for diverse CAIs from Vigarano (CV3) yield internal isochrons with a clearly resolved spread in initial <sup>26</sup>Al/<sup>27</sup>Al, meaning that CAIs formed and were reprocessed over a much longer time span. Primitive (unmelted) CAIs have a consistent value of  $5.2 \pm 0.1 \times 10^{-5}$ , melted CAIs range from  $5.17 \times 10^{-5}$  to  $4.24 \times 10^{-5}$ , and one single object with a complex multistage history has an internal range of  $^{26}\text{Al}/^{27}\text{Al} = (4.77 - 2.77) \times 10^{-5}$ . The entire range corresponds to an age span of ~0.7 Ma. Thus not all CAIs formed at “time zero”, and only the most primitive CAIs should be used as benchmarks for earliest Solar System chronology.

Published by Elsevier B.V.

## 1. Introduction

Evidence for the events, processes and conditions that existed during the nebular phase (at 4.57 Ga) of the early Solar System is preserved in primordial material within small bodies such as asteroids and comets, and which we can access in the form of meteorites and micrometeorites. Because of the brief total time span involved, 2–3 Ma, high-precision microchronology of those ancient events is difficult. The most accurate absolute chronometer is Pb–Pb, whose precision (typically <1 Ma [Amelin et al., 2002; Bouvier and Wadhwa, 2010]) is not sufficient to resolve in detail closely spaced events within the 2–3 Ma interval over which high temperature processing occurred in the solar nebula. Resolution of these events is made possible through the use of relative chronometers based on short-lived radionuclides that were present in the early Solar System, especially <sup>26</sup>Al, whose 0.705<sup>1</sup>Ma half life (Norris et al., 1983) allows a time resolution of ~10,000 years (1% of mean life) to be reached with high precision Mg isotopic data. The main evidence for live <sup>26</sup>Al in the early Solar System comes from Al-correlated excesses of its daughter product <sup>26</sup>Mg in calcium–aluminum-rich inclusions (CAIs)

in meteorites, which record the highest levels of <sup>26</sup>Al in any early Solar System materials and are the oldest Solar System objects dated by the Pb–Pb chronometer (Amelin et al., 2002; Bouvier and Wadhwa, 2010). A 1995 review (MacPherson et al., 1995) of the <sup>26</sup>Al record in CAIs showed that, while most CAIs yield a rather consistent initial <sup>26</sup>Al/<sup>27</sup>Al ratio of  $\sim 5 \times 10^{-5}$  at the time of CAI formation (the “canonical” value), on a summary histogram the data define a wide peak centered on initial <sup>26</sup>Al/<sup>27</sup>Al  $\sim 4.5 \times 10^{-5}$  and a range of variation  $(4-6) \times 10^{-5}$  corresponding to a possible time spread of 0.4 Ma. However, the width of that histogram peak was likely due to analytical uncertainty of data that mostly were collected by an older, lower precision generation of ion microprobes (SIMS—secondary ion mass spectrometers). Thus there was no possibility in 1995 of resolving any real spread in values among different CAIs, which could correlate with the nebular duration of very high temperature processing and CAI formation. Recent studies of CAIs using in-situ laser ablation multicollector inductively coupled plasma mass spectrometer (LA–ICPMS) analyses (Young et al., 2005) improved the analytical precision. However, the relatively large spot size (~50–100 μm) makes it very difficult to obtain analyses of pure single phases or of distinct chemical zones within single crystals in many phases, which reduces the precision of any isochron slopes. Mineral separates combined with high-precision solution ICP–MS are a big improvement (e.g. Jacobsen et al., 2008) over laser ablation, although there is still the likelihood of some mineral cross-contamination. With the advent of the latest generation of multicollector, large-radius SIMS, it is now possible to obtain high-precision analyses of individual phases in a well-characterized petrographic context.

\* Corresponding author. Tel.: +1 202 633 1803; fax: +1 202 357 2476.

E-mail address: [macphers@si.edu](mailto:macphers@si.edu) (G.J. MacPherson).

<sup>1</sup> Although 0.72 and 0.73 My are commonly cited values, the nuclear chemistry community generally uses 0.705 Ma, the value adopted herein. See a discussion in Kita and Ushikubo (in press).

We have analyzed a new suite of diverse CAIs from the Vigarano CV3 chondrite (chosen because its CAIs have very little secondary mineralization or shock effects), and obtained high-precision internal isochrons for each of them. We found well-resolved real variations in initial  $^{26}\text{Al}/^{27}\text{Al}$  among these CAIs, with primitive (unmelted) CAIs consistently yielding initial  $^{26}\text{Al}/^{27}\text{Al}$  ratios of  $5.2 \times 10^{-5}$  whereas highly processed (partially or completely melted) CAIs yield a range of  $(4.2\text{--}5.2) \times 10^{-5}$ .

## 2. Materials and methods

The analyzed CAIs cover a wide range of CAI types (MacPherson, 2007). Polished thin sections of each CAI were fully characterized prior to SIMS analysis. An FEI Nova NanoSEM 600 scanning electron microscope (SEM) was used to obtain backscattered electron images and X-ray elemental maps. Quantitative chemical data was collected using a JEOL JXA8900 electron microprobe. Both of these instruments are located at the Smithsonian Institution.

### 2.1. Sample descriptions

Detailed descriptions and mineralogy of all the CAIs reported herein will be given in a forthcoming separate paper. Following are summary descriptions.

USNM 3138 F1 (hereafter “F1”) is an elliptical  $\sim 4 \times 5$  mm Type B2 CAI containing melilite ( $\text{Åk}_{12-67}$ ), pyroxene (5–11 wt.%  $\text{TiO}_2$ , 16–24 wt.%  $\text{Al}_2\text{O}_3$ ), anorthite, and spinel. A minor amount of nepheline is secondary after anorthite, and occurs as very thin oriented lamellae within the latter.

USNM 3138 F4 (“F4”) is a very unusual and complex CAI (Fig. 1). It is spheroidal in shape, 4.7 mm in diameter, and has three distinct concentric zones that differ in mineralogy and texture (Fig. 2). The innermost lithology (shown in detail in Fig. 3) has the appearance of a xenolith, and consists of a rind of spinel that encloses aluminous melilite ( $\text{Åk}_{10-24}$ ), minor pyroxene and spinel, and intermediate melilite ( $\text{Åk}_{30-55}$ ) that encloses (with sharp contacts) the other phases. The aluminous melilite is rounded and irregular in shape. Exterior to the “xenolith” is a typical Type B assemblage (Fig. 2) of intermediate melilite ( $\text{Åk}_{36-68}$ ), pyroxene (“fassaite”: 15–22%  $\text{Al}_2\text{O}_3$ , 2–19%  $\text{TiO}_2$ ), anorthite, and spinel. The mantle of the inclusion (Fig. 2) is very anorthite-rich (now largely replaced by nepheline) with pyroxene and very magnesium-rich melilite ( $\text{Åk}_{66-80}$ ). Although this “Type C” assemblage exists primarily in the mantle, it also occurs in selvages within the Type B interior of the inclusion as well, particularly next to pyroxene and anorthite. This association indicates that the late-stage heating event that formed the mantle also caused partial (eutectic) melting in the interior as well. A critical observation

is that the magnesium-rich melilite in the Type C lithology and the more aluminum-rich melilite elsewhere in the CAI lie on opposite sides of the thermal minimum (at  $\sim \text{Åk}_{72}$ ) in the binary gehlenite–åkermanite system and cannot have formed from the same melt. Bulk composition determinations of the mantle relative to the interior show that there is no significant difference in magnesium but, rather, the mantle is distinctly enriched in silicon. This makes sense from a petrologic point of view, as excess silica stabilizes anorthite at the expense of gehlenite and any remaining melilite will be much more magnesium-rich. Thus we conclude silica was added to the exterior of the CAI at the time of final melting, to form the Type C lithology. This is important for interpreting the isotopic data; see Discussion section. Enveloping the entire CAI is a thick pyroxene rim that contains within it numerous tiny fragments of ferromagnesian chondrules. The pyroxene is different in composition from the interior pyroxene, containing lower total titanium ( $< 4$  wt.% as  $\text{TiO}_2$ ) and consistently elevated FeO (mostly  $> 0.3$  wt.%).

USNM 3138 F5 (“F5”) is an irregularly shaped,  $\sim 3 \times 4$  mm amoeboid olivine aggregate (Fig. 4), consisting mostly of fine-grained and highly magnesian olivine ( $\text{Fo}_{93-100}$ , mostly  $\sim \text{Fo}_{97}$ ). The olivine aggregate encloses numerous, irregularly-shaped, refractory nodules consisting of spinel rimmed by pyroxene ( $< 1\text{--}6\%$   $\text{TiO}_2$ , 2–21%  $\text{Al}_2\text{O}_3$ ). One large refractory nodule (Fig. 5) is elliptical in shape ( $\sim 320 \times 270 \mu\text{m}$ ) and consists of gehlenitic melilite ( $\text{Åk}_{2-24}$ ) that encloses fine-grained spinel and perovskite.

USNM 3138 F6 (“F6”) is a somewhat nodular compact Type A CAI (Fig. 6),  $2.2 \times 2.8$  mm, consisting mostly of melilite ( $\text{Åk}_{8-55}$ ) with greatly subordinate pyroxene (8–15%  $\text{TiO}_2$ , 17–23%  $\text{Al}_2\text{O}_3$ ) and accessory perovskite, spinel, and rhönite. The pyroxene occurs mainly as anastomosing networks that poikilitically enclose numerous equant melilite grains, a texture that suggests partial melting only slightly above the solidus. A small quantity of rhönite is present in this inclusion.

USNM 3138 F8 (“F8”) is an irregularly-shaped Fluffy Type A CAI, approximately  $1.8 \times 4.8$  mm in overall size, consisting mostly of densely crystalline melilite ( $\text{Åk}_{0-22}$ ) that encloses hibonite, spinel, and perovskite. Sparse grains of titanium-rich pyroxene (13–19%  $\text{TiO}_2$ , 22–27%  $\text{Al}_2\text{O}_3$ ) are also present. The hibonite crystals are concentrated within restricted interior regions of the CAI, and wide expanses of the CAI are hibonite-free.

USNM 3138 F9 (“F9”) is an elliptical Compact Type A CAI,  $\sim 6.2 \times 3.9$  mm, which borders on the meteorite fusion crust. It is texturally similar to F6, but it lacks rhönite and has abundant hibonite plus very fine-grained perovskite in its outer mantle (unlike F8, where the hibonite is in the interior). F9 also has far more spinel than does F6. There is no evidence of any mineralogical or textural modification of F9 even right at the fusion crust; nevertheless all isotopic analyses of F9 were done far from the fusion crust.

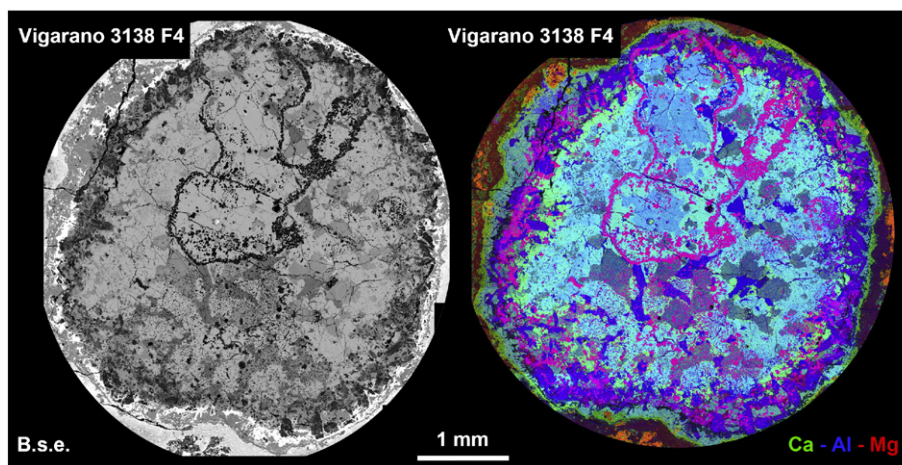


Fig. 1. Paired backscattered electron image and false-color X-ray element map of Vigarano 3138 F4. In the false color map, melilite appears sky-blue, pyroxene is olive green, anorthite is dark blue, and spinel is magenta.

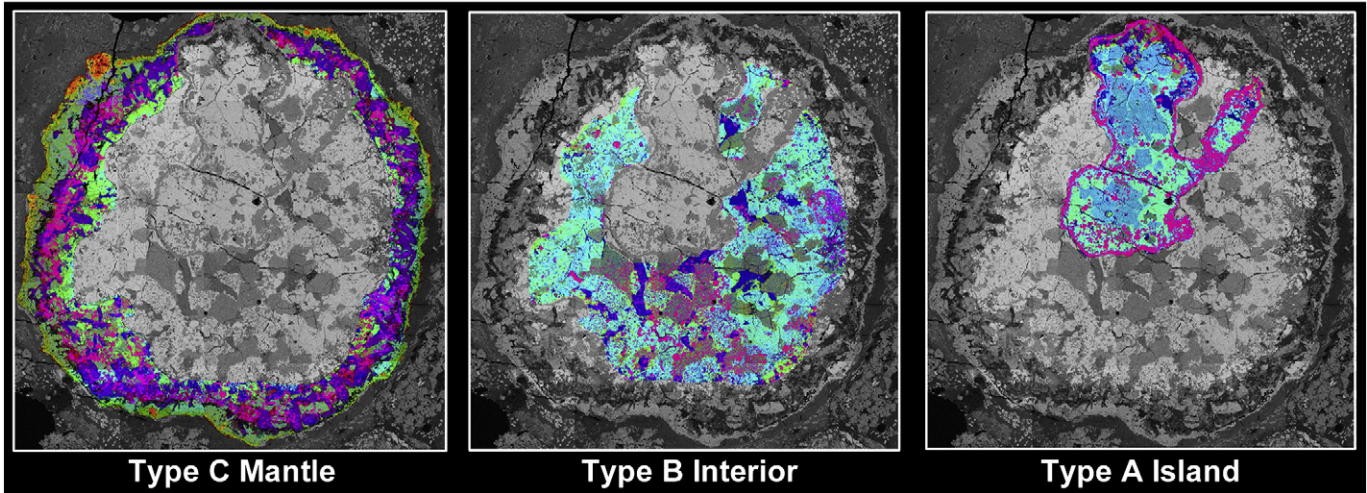


Fig. 2. False-color X-ray element maps of the three lithologic units in Vigarano 3138 F4, superimposed onto back-scattered electron images. Colors as in Fig. 1.

The Fluffy Type A (F8) and the amoeboid olivine aggregate (F5) are both highly primitive (unmelted, possibly condensate) CAIs, whereas all the others experienced partial to extensive melting.

## 2.2. CAI bulk compositions

Bulk compositional data and high-resolution backscattered electron images were obtained using the Smithsonian SEM described above, operated at 15 keV with a sample current of 2–3 nA. The SEM is equipped with a Thermo-Noran energy dispersive X-ray analytical system, and data is stored and processed using Thermo-Scientific Noran System Six software. This software allows for full-spectrum imaging, in which a complete energy-dispersive spectrum is collected and stored for each pixel within a map. Multiframe map mosaics with 10–20% frame overlap provide full coverage of large CAIs at sufficient spatial resolution to resolve grains down to  $\sim 2 \mu\text{m}$  in diameter. The bulk composition of each frame (corrected for overlap onto adjacent frames) was determined by summing the compositions for all

pixels, summing the frame compositions, and normalizing the totals to 100%. The software allows extraction of data from irregularly shaped areas, so that unwanted pixels (epoxy, cracks, meteorite matrix) can be eliminated. This feature also allows the composition of individual areas within each inclusion to be determined. Spectra were quantified using Gaussian spectrum fitting and standardless Phi-Rho-Z matrix correction. The variation in composition from frame to frame within each CAI gives a measure of internal mineralogic heterogeneity, and this was used as an estimate of precision on bulk Al/Mg ratios in the construction of Fig. 9b.

## 2.3. SIMS Al–Mg isotope analyses of CAIs

All isotopic analyses were acquired using the Cameca IMS-1280 at the University of Wisconsin–Madison (WiscSIMS [Kita et al., *in press*]), utilizing monocollection for high Al/Mg phases and multicollection with Faraday cups for low Al/Mg phases.

### 2.3.1. Multicollection Faraday cup analyses

For multicollection Faraday cup (FC) analyses, the primary  $\text{O}^-$  ion beam was adjusted to an oval shape with  $20 \mu\text{m} \times 25 \mu\text{m}$  diameter with the intensity of 7 nA (olivine and spinel) and 20 nA (melilite and fassaite). For F8, fassaite and spinel analyses were made with 7 nA ( $25 \mu\text{m}$ ) and 3 nA ( $10 \mu\text{m}$ ) primary beam conditions respectively, because of the small grain sizes in this sample. Secondary ion optics were adjusted to  $\times 200$  magnification from sample to the Field Aperture (FA,  $6000 \mu\text{m}^2$ ) with a mass resolving power (MRP) of  $\sim 2500$ , which was enough to separate both  $^{48}\text{Ca}^{++}$  and  $\text{MgH}^+$  interferences from the Mg mass spectrum. During analyses of the fassaite glass standard (10%  $\text{TiO}_2$ ), we checked tailing of peaks for  $^{24}\text{Mg}$  ( $\text{Ca}^{++}$  and  $\text{Ti}^{++}$  at lower mass) and  $^{25}\text{Mg}$  ( $^{24}\text{MgH}^+$  at higher mass). From the tailing of the Mg peaks we estimate the contribution of  $\text{Ca}^{++}$  and  $\text{Ti}^{++}$  to  $^{24}\text{Mg}$  is less than 0.0001%, and the contribution of  $\text{MgH}^+$  to  $^{25}\text{Mg}$  is less than 0.0005%. Thus the interferences are negligible.

Four multicollection FC detectors were used to detect  $^{24}\text{Mg}^+$ ,  $^{25}\text{Mg}^+$ ,  $^{26}\text{Mg}^+$  (with  $10^{11} \Omega$  resistors) and  $^{27}\text{Al}^+$  (with  $10^{10} \Omega$  resistor) ions simultaneously, set up for  $^{25}\text{Mg}$  to be nearly at the ion optical axis. Secondary  $^{24}\text{Mg}^+$  and  $^{27}\text{Al}^+$  ions intensities were at the range of  $(0.5\text{--}5) \times 10^8$  cps, depending on the major element compositions. Each analysis takes 8 min. The baseline of the FC detectors was monitored during presputtering and averaged over 8 analyses. Due to the differences in Mg secondary intensities, we ran each mineral separately. A melilite glass standard ( $\sim \text{Ak}_{67}$ ), a fassaite glass standard with 5 wt.%  $\text{TiO}_2$ , a natural spinel standard, and San Carlos olivine standard were

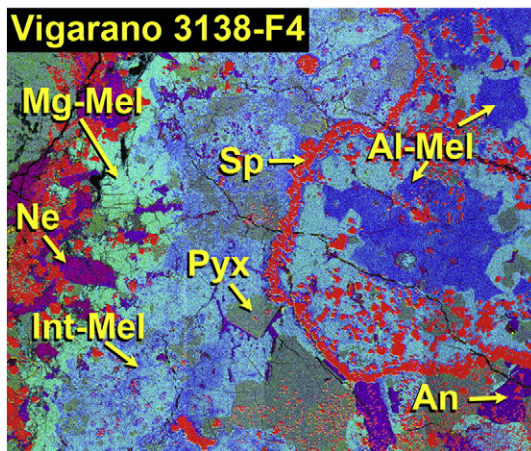


Fig. 3. False-color X-ray element map of the central “xenolith” in Vigarano 3138 F4, with the color table greatly stretched and enhanced to show the aluminum and magnesium zoning within the melilite. On the left side of the image is part of the magnesium-rich Type C mantle, showing a sharp boundary between the Mg-rich melilite (Mg-Mel) and the intermediate melilite (Int-Mel) in the interior. In this map, aluminum-rich melilite (Al-Mel) in the island is dark blue, intermediate melilite (Int-Mel) is sky blue, magnesium-rich melilite is greenish-blue, pyroxene (Pyx) is olive green, anorthite (An) is purple, nepheline (Ne) is magenta, and spinel (Sp) is red.

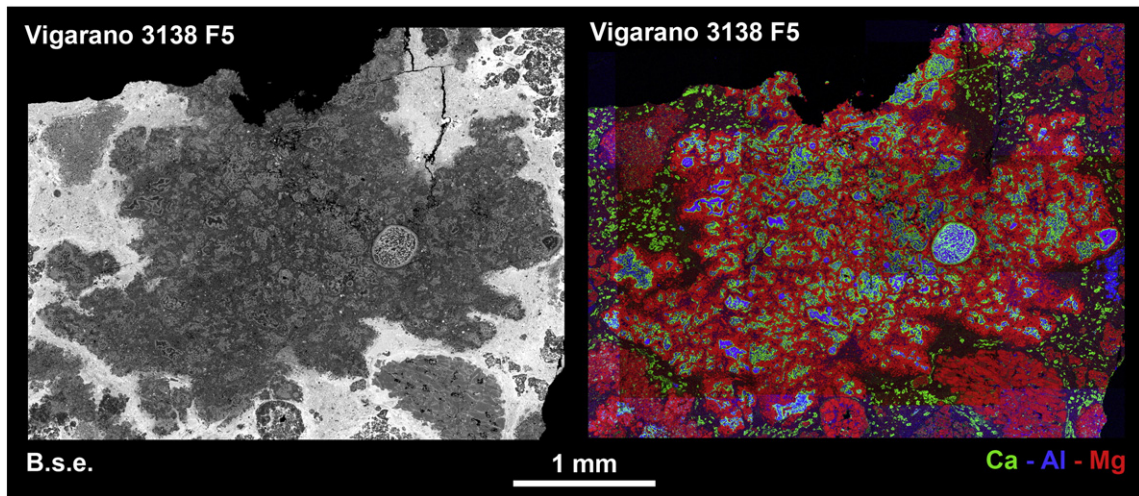


Fig. 4. Paired backscattered electron image and false-color X-ray element map of Vigarano 3138 F5. In the false color map, melilite in the small CAI nodule is sky-blue, olivine is red, pyroxene is green, and spinel is purple.

used as running standards for melilite, fassaite, spinel and olivine analysis, respectively. We also measured several melilite glass standards ( $\text{\AA}k_{15-85}$ ), synthetic melilite crystals ( $\text{\AA}k_{72}$ ,  $\text{\AA}k_{100}$ ), fassaite glass standards with various  $\text{TiO}_2$  contents (2–10%) and synthetic forsterite standard, in order to verify analytical conditions. A total of 8 sets of standard analyses were obtained by bracketing 8–10 unknown sample analyses and the average of 8 standard analyses were used to correct instrumental bias on the measured Mg isotope ratios.

The isotope mass fractionation correction (both instrumental and natural) is applied to measured Mg isotope ratios to estimate excess  $^{26}\text{Mg}$ . The fractionation-corrected  $\delta^{26}\text{Mg}^*$  values were calculated using an exponential law with slope of 0.514 from the evaporation experiment of Davis et al. (2005). Both internal errors and the external reproducibility of fractionation-corrected  $\delta^{26}\text{Mg}^*$  values for standards were typically 0.03–0.05‰ ( $2\sigma$ ) for fassaite glass, spinel and forsterite standards and 0.07–0.20‰ ( $2\sigma$ ) for  $\text{\AA}k_{65}$ – $\text{\AA}k_{15}$  glass standard. The external reproducibility of bracket standards are propagated to the uncertainties of  $\delta^{26}\text{Mg}^*$  values of the sample analyses. The reproducibility of the measured  $^{27}\text{Al}/^{24}\text{Mg}$  ratios of the running standard was better than 1% ( $2\sigma$ ) for melilite and spinel, ~5% ( $2\sigma$ ) for multiple fassaite glass standards with a range of major element compositions, and ~10% ( $2\sigma$ ) for the San Carlos olivine standard (although the Al/Mg ratio of San Carlos olivine is so low that the reproducibility is not really important). These uncertainties are assigned

as those of  $^{27}\text{Al}/^{24}\text{Mg}$  ratios of CAI data, while the internal precision of  $^{27}\text{Al}/^{24}\text{Mg}$  ratios in the individual analyses is much better than 1%.

### 2.3.2. Monocollection electron multiplier mode

For monocollection electron multiplier (EM) analyses in pulse counting mode, the primary  $\text{O}^-$  ion beam was adjusted to the oval shape with  $4 \times 6 \mu\text{m}$  diameter with the intensity of 70 pA for melilite and 140 pA for anorthite analyses. The instrument conditions are similar to that of multi-FC analyses, except for using smaller FA ( $4000 \mu\text{m}^2$ ) and MRP of 3500. Three Mg isotopes ( $^{24}\text{Mg}^+$ ,  $^{25}\text{Mg}^+$ ,  $^{26}\text{Mg}^+$ ) were detected using monocollection EM by magnetic field switching, while  $^{27}\text{Al}^+$  was detected using FC detector on the multi-collection system with a  $10^{11} \Omega$  resistor during the collection of  $^{25}\text{Mg}^+$ . Dead time of the EM detector was 19 ns. The intensity of  $^{24}\text{Mg}^+$  ions was typically at  $3 \times 10^4$  cps for the analyses of CAI minerals, while it was as low as  $4 \times 10^3$  cps for anorthite with high  $^{27}\text{Al}/^{24}\text{Mg}$  ratios ( $>1000$ ). A single analysis consists of 100 cycles of collecting Mg and Al isotope signals, which takes 1 h. Al-rich melilite glass standards, anorthite glass standards and labradorite mineral standards with known Mg contents were analyzed for the correction of the instrumental biases on Al–Mg measurements. Both internal errors and the reproducibility of fractionation-corrected  $\delta^{26}\text{Mg}^*$  values for melilite glass standard ( $\text{\AA}k_{35}$ ) were better than 1%, while internal precisions of sample analyses were between 1% and 15% that depend on the Mg contents in the samples. Relative sensitivity factors of SIMS  $^{27}\text{Al}/^{24}\text{Mg}$  ratios in melilite and anorthite are estimated from glass standard with known Al and Mg concentrations with a precision of 1%. For the CAI samples, several analyses show significant decrease in measured  $^{27}\text{Al}/^{24}\text{Mg}$  ratios during a spot analysis. In such cases, we observed  $\mu\text{m}$ -scale Mg hot spots in the direct ion image of  $^{24}\text{Mg}^+$ , which indicates contamination by micron-scale Mg-rich inclusions. These analyses were rejected, because  $^{24}\text{Mg}^+$  intensities increased above the optimized range for the EM detector ( $<10^5$  cps).

The data are plotted in several figures as  $\delta^{26}\text{Mg}^*$  vs.  $^{27}\text{Al}/^{24}\text{Mg}$ , where

$$\delta^{26}\text{Mg}^* = \delta^{26}\text{Mg} - \left[ \left( \frac{\delta^{25}\text{Mg}}{1000} + 1 \right)^{1/0.514} - 1 \right] \times 1000, \quad (1)$$

where

$$\delta^{25}\text{Mg} = \left[ \frac{(^{25}\text{Mg}/^{24}\text{Mg})_{\text{samp}}}{(^{25}\text{Mg}/^{24}\text{Mg})_{\text{std}}} - 1 \right] \times 1000 \quad \text{and} \quad \delta^{26}\text{Mg} = \left[ \frac{(^{26}\text{Mg}/^{24}\text{Mg})_{\text{samp}}}{(^{26}\text{Mg}/^{24}\text{Mg})_{\text{std}}} - 1 \right] \times 1000. \quad (2)$$

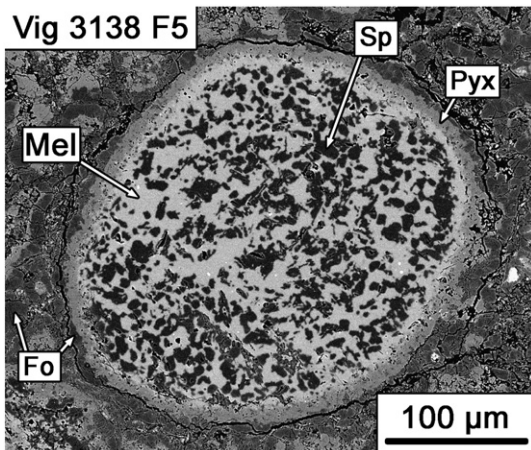


Fig. 5. Backscattered electron image of the small round CAI contained within the amoeboid olivine aggregate Vigarano 3138 F5. Note that olivine crystals grew directly on the surface of the CAI; they are not simply in physical juxtaposition within an aggregate. Abbreviations as used previously except: Fo—forsterite.

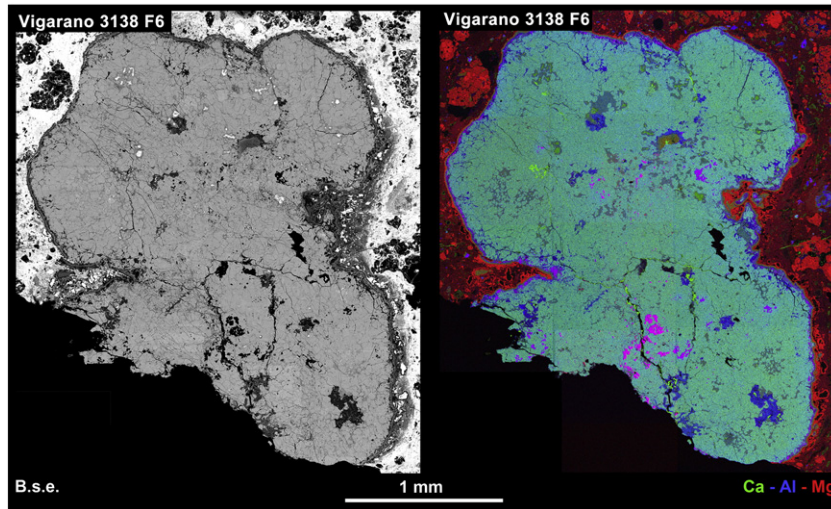


Fig. 6. Paired backscattered electron image and false-color X-ray element map of the compact Type A CAI Vigarano 3138 F6. Abbreviations as used previously.

### 3. Results

All data are tabulated in Appendix Table A1, and shown graphically in Fig. 7. The primitive CAIs F5 and F8 both yield well defined isochrons (Fig. 7a,b) corresponding to initial  $^{26}\text{Al}/^{27}\text{Al} = (5.13 \pm 0.11) \times 10^{-5}$  (F5) and  $(5.29 \pm 0.28) \times 10^{-5}$  (F8). These values are very close to that given by an isochron of bulk CAIs from the Allende CV chondrite  $(5.23 \pm 0.13) \times 10^{-5}$ ; Jacobsen et al., 2008). Olivine in F5 also yields a very accurate value for initial  $\delta^{26}\text{Mg}^*_0 = -0.020 \pm 0.015\%$ . In the Type B2 CAI F1 (Fig. 7c), data from melilite, pyroxene, and most spinel yield an isochron corresponding to initial  $^{26}\text{Al}/^{27}\text{Al} = (4.66 \pm 0.17) \times 10^{-5}$ , with some scattering from the isochron slope (MSWD = 4.8). However, anorthite in F1 has almost completely lost its excess  $^{26}\text{Mg}$  (inset to Fig. 7c), and  $^{27}\text{Al}/^{24}\text{Mg}$  extends to much higher values (~1900) than expected for pristine igneous anorthite in Type B CAIs (200–400 [Kita et al., in press]). Moreover, whereas spinel enclosed in melilite and pyroxene plot on the isochron, all spinel enclosed in anorthite plots well above the isochron (Fig. 7c). This observation suggests magnesium isotope exchange between anorthite and spinel after  $^{26}\text{Al}$  had decayed, but not between spinel and either melilite or pyroxene. The two Compact Type A CAIs F6 and F9 are nearly identical in mineralogy and texture, yet they yield two distinctly different isochron slopes (Fig. 7d,e) corresponding to initial  $^{26}\text{Al}/^{27}\text{Al} = (4.24 \pm 0.36) \times 10^{-5}$  (F6) and  $(5.17 \pm 0.31) \times 10^{-5}$  (F9). Finally, CAI F4 is a composite object, containing a Type A xenolith enclosed in a Type B that in turn is enclosed within a silica-rich (anorthite-normative) mantle that also contains chondrule fragments in its outermost regions (Fig. 2). Aluminum-rich melilite and spinel in the Type A xenolith yields an isochron (Fig. 7f) corresponding to initial  $^{26}\text{Al}/^{27}\text{Al} = (4.77 \pm 0.31) \times 10^{-5}$ . Pyroxene and magnesium-rich melilite in the outermost mantle yield a very different isochron with a shallower slope (Fig. 7f) corresponding to initial  $^{26}\text{Al}/^{27}\text{Al} = (2.77 \pm 0.77) \times 10^{-5}$  and elevated initial  $^{26}\text{Mg}/^{27}\text{Al} = (0.52 \pm 0.12)$ . Although different in detail, the petrologic and isotopic diversity and complexity of F4 are reminiscent of Allende CAI USNM 5241 that was studied by Hsu et al. (2000).

### 4. Discussion

#### 4.1. Primitive CAIs and true Solar System initial

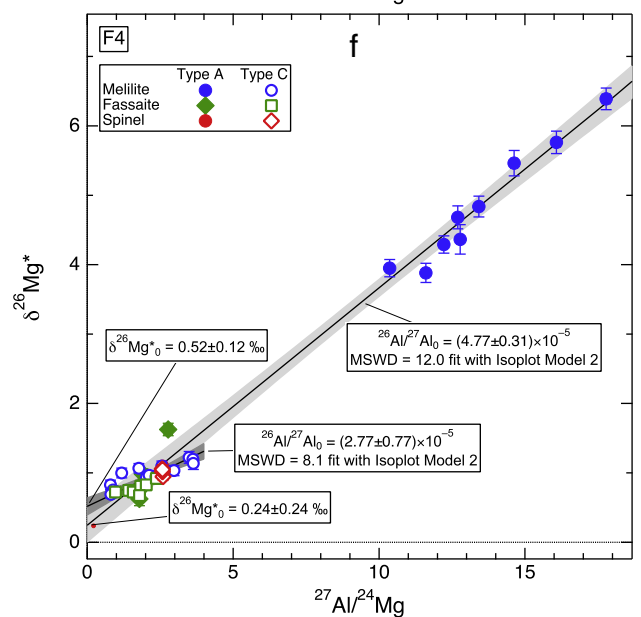
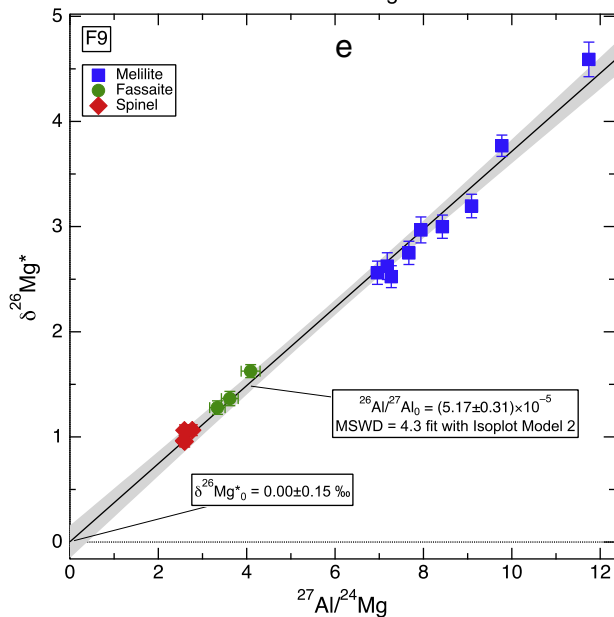
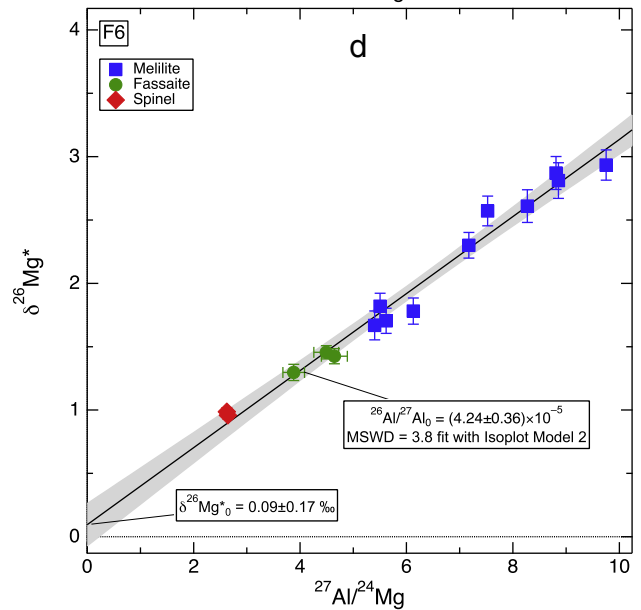
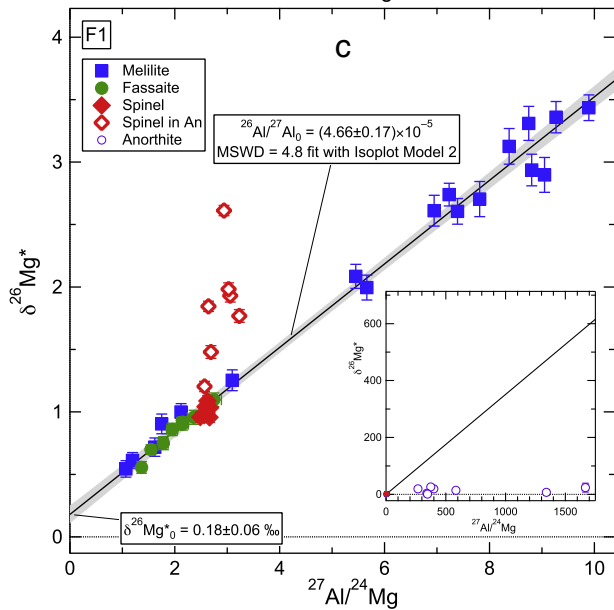
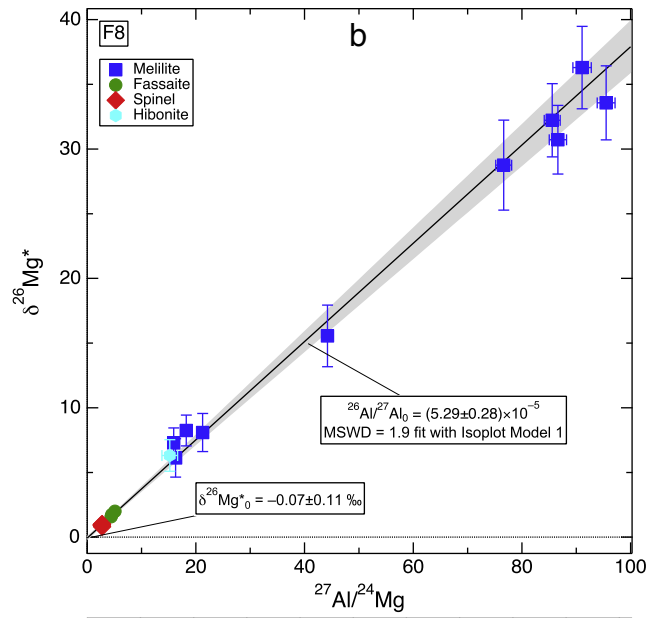
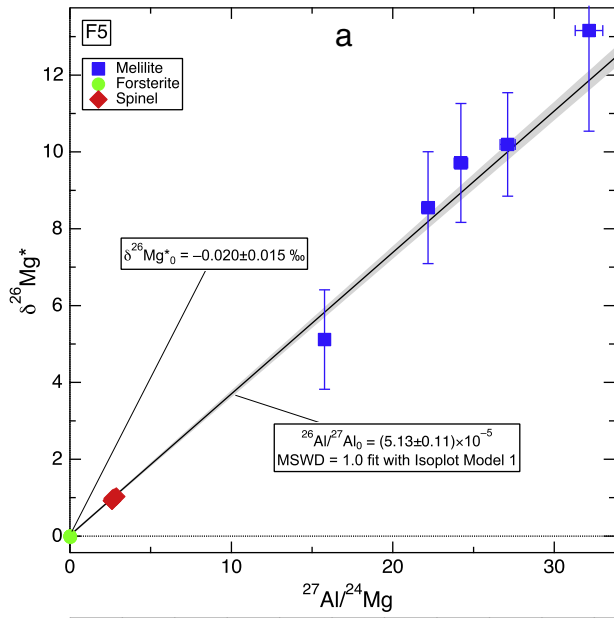
The CAIs in this study fall into two basic categories, primitive and highly reprocessed, based on their petrologic properties. F8 and F5 are both very irregular in shape and have the attributes of aggregates.

Although some post-aggregation heating cannot be entirely ruled out, it is certain that these two objects were never melted. All the other CAIs have rounded to spheroidal shapes, and their mineralogy and textures are broadly consistent with what would be expected for solidified partial melts having the relevant bulk compositions. CAI F4, at least, probably was melted and remelted several times. Thus, whereas the two primitive CAIs F5 and F8 retain many of the attributes of their condensate precursors, the other objects have been severely reheated and partially to completely melted at some time subsequent to the formation of their precursors. It is this time difference that is of interest here, because it addresses the question of how long CAIs were being formed and reprocessed in the solar nebula. CAIs are generally regarded as the first objects formed in the Solar System, and the unspoken assumption is that all CAIs collectively represent an instant in time: they are all the same age. Our observation that the two primitive CAIs F5 and F8 yield initial  $^{26}\text{Al}/^{27}\text{Al}$  values very close to one another (Fig. 7) and to the whole-CAI value of  $(5.23 \pm 0.13) \times 10^{-5}$  suggests that the time period between primordial fractionation of Mg from Al (presumably by condensation) and first CAI formation was very short, less than a few tens of thousands of years. A third primitive CAI (MacPherson et al., 2010) also yielded a similar initial  $^{26}\text{Al}/^{27}\text{Al}$  value of  $(5.27 \pm 0.17) \times 10^{-5}$ .

#### 4.2. Extended reprocessing of igneous CAIs

However, the highly processed (partially melted) CAIs exhibit a clear range of initial  $^{26}\text{Al}/^{27}\text{Al}$ , from  $4.24 \times 10^{-5}$  to  $5.17 \times 10^{-5}$ . Final remelting of the composite CAI F4, possibly in the chondrule-forming region, extends this range down to  $2.77 \times 10^{-5}$ . Melting of CAIs thus continued nearly  $2 \times 10^5$  years after initial CAI formation (Fig. 8), and remelting of F4 in the chondrule forming region took place ~0.7 Ma after initial CAI formation. Hsu et al. (2000) reached a similar conclusion for another complex Type B CAI, USNM 5241 (Allende), which experienced remelting ~0.4 Ma after initial CAI formation.

The three CAIs (F1, F4, and F6) that have initial  $^{26}\text{Al}/^{27}\text{Al}$  ratios significantly lower than  $5.2 \times 10^{-5}$  all show elevated initial  $\delta^{26}\text{Mg}^*_0$  values, from 0.1 to 0.5‰ (in the case of the F4 outer mantle). These elevated initial  $\delta^{26}\text{Mg}^*_0$  values are consistent with melting or remelting of a refractory precursor at a sufficient time after initial Al/Mg fractionation (e.g., condensation) that their average bulk compositions acquired measurable excess radiogenic  $^{26}\text{Mg}$ , since melting homogenizes magnesium isotopic composition. All four melted CAIs (i.e. including F9) show resolvable scatter from the linear regression on the isochron diagram, as indicated by mean square weighted



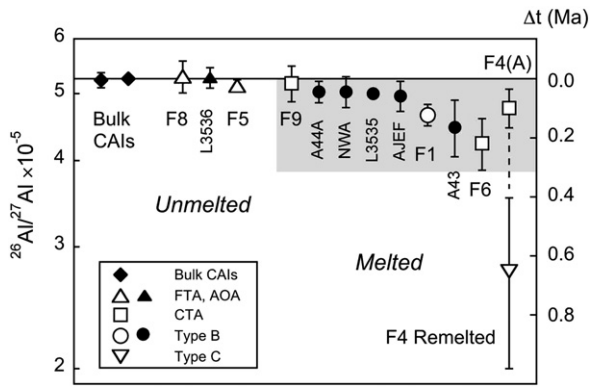


**Fig. 8.** Initial  $^{26}\text{Al}/^{27}\text{Al}$  ratios of all CAIs for which high-precision internal isochron data exist, showing that primitive CAIs all are close to  $5.2 \times 10^{-5}$  (Solar System initial, SSI) whereas partially or completely melted CAIs exhibit a well-resolved range, corresponding to a time interval of 0.2 Ma (not counting final remelting of F4). Open symbols are from this work and filled symbols are literature data. Sources: L3536 = Leoville 3536-1 from MacPherson et al. (2010); L3535 = Leoville 3535-1 from Kita et al. (in press); NWA = Northwest Africa 2364 from Bouvier and Wadhwa (2010); A43, A44a, and AJEF are three Allende CAIs from Jacobsen et al. (2008).

deviations (MSWD) of  $\geq 4$ , and which are significantly larger than those of the unmelted CAIs (MSWD  $\leq 2$ ). The relatively large scatter of the data for the melted CAIs from the linear regressions implies incomplete isotopic homogenization and perhaps incomplete melting of the refractory precursors.

#### 4.3. Primitive vs. reprocessed CAIs: What is true Solar System initial?

The narrow range of initial  $^{26}\text{Al}/^{27}\text{Al}$  ratios of the unmelted CAIs, which is identical to that of the whole CAI isochron (Jacobsen et al., 2008), indicates that primary condensation of refractory solids from a hot nebular gas occurred within a short time scale,  $<0.1$  Ma and possibly  $<20$  Ky. In contrast, our data for the compact Type A and B2 CAIs show that subsequent CAI melting events occurred over an interval of at least 0.2 Ma, meaning that the crystallization ages of CAIs (especially melted ones) cannot necessarily be equated with condensation ages. Thus we recommend that chronology studies of CAIs aimed at measuring the age of the Solar System based on other isotope systems, especially those relying on internal isochrons, should focus mainly on the primitive types, such as Fluffy Type As, fine-grained spinel-rich inclusions, and amoeboid olivine aggregates, as these are the ones that record the beginnings of CAI formation. Studies based on whole-CAI measurements are less sensitive to this issue, provided that the CAIs largely were closed systems during any melting or other reprocessing.

The debate over what constitutes a precise value for Solar System initial  $^{26}\text{Al}/^{27}\text{Al}$  is now converging on a consistent refined value,  $(5.20 \pm 0.10) \times 10^{-5}$ , based on a weighted average of the value derived from high-precision ICP-MS whole-CAI measurements (Jacobsen et al., 2008) plus the internal isochrons derived from SIMS isotope data for F8 and F5 (this study) and Leoville 3536-1 (MacPherson et al., 2010). There is no compelling evidence for much higher, pre-CAI “supracanonical” value (Thrane et al., 2006) and the group reporting most of the supracanonical data has recently reported an initial  $^{26}\text{Al}/^{27}\text{Al}$  value of  $(5.25 \pm 0.02) \times 10^{-5}$ , for several CAIs and AOAs from the Efremovka CV chondrite (Larsen et al., 2011).

#### 4.4. Mg/Al fractionation in CAIs

Normal, non-FUN CAIs are usually enriched in the heavy isotopes of magnesium and silicon, and efforts to model these fractionation effects

coupled with depletions in bulk Mg/Al bulk ratios generally have assumed that both originated from major evaporative mass loss of relatively volatile magnesium and silicon relative to refractory calcium and aluminum during one or more melting events (Richter et al., 2002, 2006). However, other studies (Jacobsen et al., 2008) based on  $^{26}\text{Al}/^{26}\text{Mg}$  systematics of bulk CAIs have concluded that the major Mg/Al fractionation observed in at least some CAIs must have predated the last melting event.

An independent way of approaching the Mg/Al fractionation problem involves consideration of the evolution of the ratio of daughter to nonradiogenic isotopes, an approach that has long been used in cosmochemistry for other systems (especially  $^{87}\text{Rb}$ – $^{87}\text{Sr}$  [Gray et al., 1973; Podosek et al., 1991]). Recent improvements in analytical precision have enabled the use of this technique for magnesium in bulk samples (Villeneuve et al., 2009). Our  $^{26}\text{Al}$ – $^{26}\text{Mg}$  isochron data is also sufficiently precise to permit determining not just the timing of the last melting event (from the slope of the isochron) but also the timing of the last significant bulk Mg/Al fractionation event by modeling the evolution of  $^{26}\text{Mg}/^{24}\text{Mg}$ . In evaluating our own data, we make two key assumptions: that the magnesium isotopic composition of the Solar System was homogeneous before  $^{26}\text{Al}$  decay; and that  $^{26}\text{Al}/^{27}\text{Al}$  was homogeneous throughout the early Solar System at a value of  $(5.23 \pm 0.13) \times 10^{-5}$ . The initial magnesium isotopic composition of the Solar System ( $\delta^{26}\text{Mg}^*_0 = -0.038\%$ , where  $\delta^{26}\text{Mg}^*_0$  is the isochron intercept) is calculated from: (a) the magnesium isotopic composition of the Earth ( $\delta^{26}\text{Mg}^*_{\text{Earth}} \equiv 0\%$ ); (b) the  $^{27}\text{Al}/^{24}\text{Mg}$  ratio of the Solar System, 0.1011, inferred from CI chondrites (Lodders et al., 2009); and (c) the early Solar System initial  $^{26}\text{Al}/^{27}\text{Al}$  ratio. In correcting our data for mass fractionation, we used an exponential fractionation law with an exponent of 0.514 derived from laboratory evaporation experiments (Davis et al., 2005). Changing the exponent from 0.514 to the commonly used value of 0.511 does not move  $\delta^{26}\text{Mg}^*_0$  values more than 0.03% for most of the CAIs. For F1, F6, and F9,  $\delta^{26}\text{Mg}^*_0$  values move by  $\sim 0.1\%$  to lower  $\delta^{26}\text{Mg}^*_0$  values by using an exponent of 0.511, due to their heavy isotope enrichments (5–9% in  $\delta^{25}\text{Mg}$ ; Table A1), though the amounts of shift are comparable to the uncertainties of the intercepts derived from the isochron regression.

The basic principles of the method are illustrated in Fig. 9a. Consider a hypothetical CAI that presently has an  $^{27}\text{Al}/^{24}\text{Mg}$  ratio of 5, a  $^{26}\text{Al}$ – $^{26}\text{Mg}$  isochron with a slope (initial  $^{26}\text{Al}/^{27}\text{Al}$  ratio) of  $3.58 \times 10^{-5}$ , indicating melting and resetting of the  $^{26}\text{Al}$ – $^{26}\text{Mg}$  system 400,000 years after formation of the precursor at  $^{26}\text{Al}/^{27}\text{Al} = 5.23 \times 10^{-5}$ , and bulk magnesium isotopic mass fractionation consistent with loss of 60% of its initial magnesium (thus the  $^{27}\text{Al}/^{24}\text{Mg}$  ratio before the evaporation event was 2). We consider three possibilities: (1) the Mg/Al evaporative fractionation event occurred when the precursor to the CAI formed, when  $^{26}\text{Al}/^{27}\text{Al} = 5.23 \times 10^{-5}$ ; (2) the Mg/Al fractionation event occurred when the CAI last melted, when  $^{26}\text{Al}/^{27}\text{Al} = 3.58 \times 10^{-5}$ ; or, (3) the Mg/Al fractionation event occurred 200,000 years before the final melting event, when  $^{26}\text{Al}/^{27}\text{Al} = 4.33 \times 10^{-5}$ . Fig. 9a gives the magnesium isotopic evolution paths for these three cases. The nearly horizontal line describes magnesium isotopic evolution of the bulk Solar System, which connects the Earth ( $^{26}\text{Al}/^{27}\text{Al} = 0$ ,  $\delta^{26}\text{Mg}^*_0 = 0\%$ ) and the early Solar System value ( $^{26}\text{Al}/^{27}\text{Al} = 5.23 \times 10^{-5}$ ,  $\delta^{26}\text{Mg}^*_0 = -0.038\%$ ) and has  $^{27}\text{Al}/^{24}\text{Mg} = 0.1016$ . Also shown are isotopic evolution lines for reservoirs with  $^{27}\text{Al}/^{24}\text{Mg}$  ratios of 2 and 5. For Case 1, the CAI will evolve along the evolution line for  $^{27}\text{Al}/^{24}\text{Mg} = 5$ , because this was the ratio established when the CAI precursor formed. For Case 2, the CAI will evolve along the evolution line for  $^{27}\text{Al}/^{24}\text{Mg} = 2$ , because this was the ratio of the CAI precursor prior to the melting event at  $^{26}\text{Al}/^{27}\text{Al} = 3.58 \times 10^{-5}$ . Case 3 is more complex: the CAI evolves along the  $^{27}\text{Al}/^{24}\text{Mg} = 2$  evolution line for 200,000 years, experiences an

**Fig. 7.** Al–Mg isochron diagrams for: the primitive unmelted CAIs (a) F5, amoeboid olivine aggregate and (b) F8, fluffy Type A; the simple melted CAIs (c) F1, Type B, (d) F6, compact Type A, and (e) F9, compact Type A; and the complex, multiply melted CAI (f) F4. Isochrons are shown with their  $2\sigma$  error bounds. All panels are drawn with the same aspect ratio, so differences in isochron slopes are readily seen.

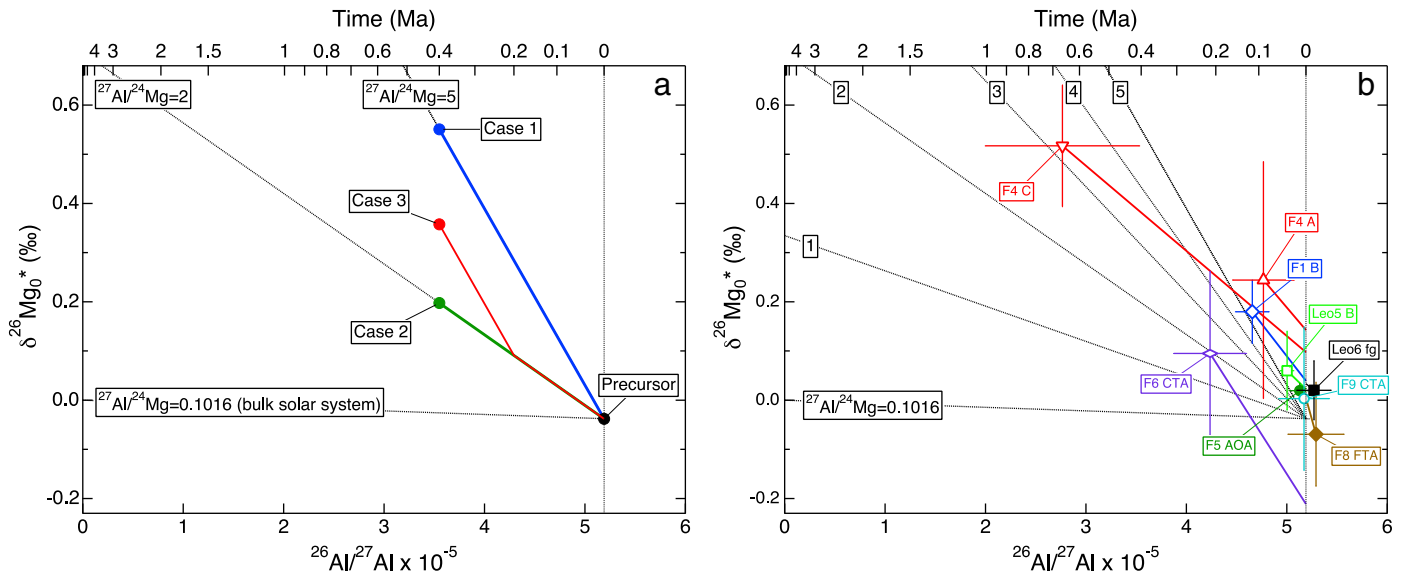


**Fig. 9.** Magnesium isotope evolution of CAIs. (a) Magnesium isotopic evolution diagram showing the effects of Mg/Al fractionation at different times (see text); (b) Vigarano CAI data plotted as in (a). Melted CAIs are depicted by open symbols and primitive ones by closed symbols. Melted CAIs are the same age or younger than primitive ones. A line is drawn from each CAI data point to the early Solar System  $^{26}\text{Al}/^{27}\text{Al}$  ratio,  $5.23 \times 10^{-5}$ , with the slope determined from the measured (present day) bulk  $^{27}\text{Al}/^{24}\text{Mg}$  ratio. AOA—amoeboid olivine aggregate; CTA—compact Type A; FTA—fluffy Type A; B—Type B; fg—fine-grained.

evaporation event that increases the  $^{27}\text{Al}/^{24}\text{Mg}$  to 5 and then evolves along a  $^{27}\text{Al}/^{24}\text{Mg} = 5$  line (parallel to the Case 1 line, but beginning at the position of the fractionation event) for the remaining 200,000 years.

Our own data are plotted in Fig. 9b. In plotting our data, the isochron for each CAI yields the  $^{26}\text{Al}/^{27}\text{Al}$  and  $\delta^{26}\text{Mg}_0^*$ , and quantitative energy-dispersive X-ray area mapping of each CAI gives the bulk chemical composition (Bullock and MacPherson, 2008; Bullock et al., 2007). The current  $^{27}\text{Al}/^{24}\text{Mg}$  for each CAI gives the slope of a magnesium isotope evolution line extrapolated backwards in time from the inferred individual CAI  $^{26}\text{Al}/^{27}\text{Al}$  ratios to the early Solar System value of  $5.23 \times 10^{-5}$ . The lines leading from each data point should either end at the Solar System initial composition (for a Case 1 type evaporation history) or to significantly negative  $\delta^{26}\text{Mg}_0^*$  (for Case 2 or 3 type evaporation histories). Note that although the analytical uncertainties on the bulk compositions are small, internal mineralogical heterogeneity within each CAI is much more significant in terms of Al/Mg. Thus there is a significant uncertainty in the slopes of the extrapolated magnesium evolution lines. Our estimate of this uncertainty is based on the variances observed between the individual tiles of the mosaics from which the bulk compositions were determined. Three of our CAIs, the two unmelted ones (F5 and F8) and the Compact Type A F9, plot essentially at the Solar System initial composition so there are no evolution curves. Vigarano CAI F1 is consistent with a Case 1 history, implying that its heavy mass-dependent isotopic fractionation and its Mg/Al ratio were established when the precursor was formed rather than when the CAI was last melted. CAI F6, a compact type A CAI that was likely melted, is somewhat ambiguous. Its current  $^{27}\text{Al}/^{24}\text{Mg}$  gives a steep magnesium evolution curve that does not intersect the early Solar System value, but in fact it is broadly consistent within error of the other CAIs. Thus although it could be explained in terms of either a Case 2 or Case 3 history, doing so likely would be overinterpreting the data. Inclusion F4 is complicated, as it has an enclave of Type A mineralogy (the “island”) enclosed within (successively) Type B and Type C material. The F4-Type A lithology has a high positive  $\delta^{26}\text{Mg}_0^*$  associated with a large relative error, so within error it is consistent with a Case 1 history. The F4-Type C lithology is significantly younger than the other CAIs plotted here, and it has a very large positive  $\delta^{26}\text{Mg}_0^*$ . It is not consistent with any of the evaporation histories shown in Fig. 9a: because the composition of the magnesium-rich melilite in the Type C lithology lies on the opposite

side of the binary minimum from that of the aluminum-rich melilite in the Types A and B lithologies, it (the Type C melilite) cannot have crystallized from the same melt. The Type C lithology requires the addition of silicon to the Type A or B melt, which stabilized anorthite and magnesium-rich melilite at the expense of more gehlenitic melilite. Therefore the CAI must have evolved along a steeper line than that shown, more like Al/Mg  $\sim 3$  and which would extrapolate back close to the Solar System initial composition. Thus for all CAIs studied herein (except possibly F6) and including even the mantle of F4, the observed Mg/Al fractionation occurred at the time of the canonical  $^{26}\text{Al}/^{27}\text{Al}$  ratio, not when the CAI last melted. This treatment of the Mg isotopic data holds together remarkably well and implies that both the  $^{26}\text{Al}/^{27}\text{Al}$  ratio and the initial Mg isotopic composition were remarkably uniform and are consistent with chondrules and the bulk Earth (Villeneuve et al., 2009).

#### 4.5. A cautionary tale about spinel

The finding of isotopically disturbed spinels enclosed within anorthite in F1 dispels a commonly held view that spinels are among the best minerals in which to look for primary isotopic signatures. This view derives in part from the results of numerous oxygen isotopic studies where spinel is indeed highly resistant to change due to the low diffusion rate of oxygen in that phase. But our work is consistent with experimental diffusion coefficient measurements (Ito and Ganguly, 2009; Liermann and Ganguly, 2002; Sheng et al., 1992) of CAI phases that demonstrated spinel to be similar to anorthite in its relatively fast magnesium diffusion behavior. The compounding problem for spinel, unlike most other CAI minerals, is that it generally is enclosed within other phases. Thus the diffusion properties of spinel alone do not control whether it exchanges, but also those of the enclosing phases. It requires a ready magnesium donor. Spinel enclosed in anorthite will readily exchange its magnesium, but spinel enclosed in melilite or pyroxene – whose diffusion coefficients are much slower than those of spinel – mostly will not.

## 5. Conclusions

High precision SIMS measurements of magnesium isotopic compositions of diverse CAIs from the Vigarano CV3 chondrite yield a

range of initial  $^{26}\text{Al}/^{27}\text{Al}$  ratios for the early Solar System. Primitive, unmelted CAIs give consistent values of  $(5.1\text{--}5.3)\times 10^{-5}$ , consistent with whole-CAI isochron studies such as that of Jacobsen et al. (2008). This value is properly regarded as true Solar System initial. However, melted and partially-melted CAIs give a more extended range, with some being close to the primitive value just stated and others having much lower values that indicate remelting as long as  $2\times 10^5$  years after the most primitive CAIs. Thus our results are consistent with the idea of a very short initial CAI formation interval, possibly less than 20,000 years, yet our data also indicate that the reprocessing of CAIs continued on far after primary CAI formation (~condensation) had ceased. One CAI experienced remelting in a region where chondrules were being formed, and this event took place  $\sim 0.7\times 10^6$  years after formation of the most primitive CAIs.

### Additional information

The authors declare no competing financial interests.

### Appendix A

**Table A1**

Magnesium isotopic data for Vigarano CAIs. Errors are  $2\sigma$ .

CAI name	Analyses #	Analyses spot	Phase analysis (*1)	$^{27}\text{Al}/^{24}\text{Mg}$	$2\sigma$	$\delta^{26}\text{Mg}^*$ (‰)	$2\sigma$ (‰)	$\delta^{25}\text{Mg}$ (‰)	$2\sigma$ (‰)	Isochron fit (*2)
3138 F1	20090417-02&03	3138 F1 area 2 An-1	An-EM	585	16	14.3	4.8	6.9	2.8	
	20090417-04&05	3138 F1 area 2 An-2	An-EM	399	17	19.5	5.5	4.5	2.7	
	20090417-06	3138 F1 area 2 An-3	An-EM	374	11	26.2	4.9	3.1	2.6	
	20090417-08	3138 F1 area 1 An-1	An-EM	267	3	19.7	2.6	2.4	1.3	
	20090417-09	3138 F1 area 4 An-2	An-EM	1667	26	23.6	15.6			
	20090417-10	3138 F2(*3) area 2 An-1	An-EM	1341	23	7.3	9.0	1.9	4.8	
	20090417-11	3138 F2 area 2 An-2	An-EM	341	7	3.9	4.8	3.4	2.9	
	20090417-12	3138 F2 area 2 An-3	An-EM	346	8	1.1	6.3	8.7	3.4	
	20090902-8	3138 F1 Area-6 UW-Mel-1	Mel	7.81	0.06	2.70	0.14	2.04	0.10	Y
	20090902-9	3138 F1 Area-6 UW-Mel-2	Mel	9.89	0.08	3.44	0.10	2.17	0.10	Y
	20090902-10	3138 F1 Area-6 UW-Mel-2	Mel	7.23	0.06	2.74	0.09	2.37	0.10	Y
	20090902-11	3138 F1 Area-2 UW-Mel-3	Mel	8.75	0.07	3.31	0.14	5.46	0.10	Y
	20090902-22	3138 F1 Area-2 UW-Mel-7	Mel	1.62	0.01	0.72	0.07	5.93	0.31	Y
	20090902-23	3138 F1 Area-8 UW-Mel-1	Mel	5.45	0.04	2.08	0.10	2.57	0.31	Y
	20090902-24	3138 F1 Area-7 UW-Mel-1	Mel	9.27	0.07	3.36	0.13	1.61	0.31	Y
	20090902-25	3138 F1 Area-7 UW-Mel-2	Mel	1.75	0.01	0.90	0.08	4.42	0.31	Y
	20090902-26	3138 F1 Area-3 UW-Mel-1	Mel	1.19	0.01	0.61	0.06	5.90	0.31	Y
	20090902-27	3138 F2 Area-4 UW-Mel-1	Mel	9.05	0.07	2.90	0.14	1.16	0.31	Y
	20090902-28	3138 F2 Area-4 UW-Mel-2	Mel	8.38	0.07	3.13	0.14	0.69	0.31	Y
	20090902-29	3138 F2 Area-4 UW-Mel-3	Mel	8.80	0.07	2.94	0.13	1.10	0.31	Y
	20090902-30	3138 F2 Area-1 UW-Mel-1	Mel	1.07	0.01	0.54	0.07	5.53	0.31	Y
	20090902-31	3138 F2 Area-1 UW-Mel-2	Mel	3.09	0.02	1.25	0.08	5.69	0.31	Y
	20090902-32	3138 F2 Area-1 UW-Mel-3	Mel	5.66	0.04	2.00	0.10	5.46	0.31	Y
	20090902-33	3138 F2 Area-1 UW-Mel-4	Mel	6.95	0.05	2.61	0.12	5.89	0.31	Y
	20090902-34	3138 F2 Area-9 UW-Mel-1	Mel	2.12	0.02	1.00	0.07	5.31	0.31	Y
	20090902-35	3138 F2 Area-9 UW-Mel-2	Mel	7.39	0.06	2.61	0.10	5.10	0.31	Y
	20090905-21	3138 F1 Area-2 UW-Px-2	Fas	1.95	0.10	0.86	0.05	6.45	0.15	Y
	20090905-22	3138 F1 Area-2 UW-Px-3	Fas	2.15	0.11	0.92	0.04	6.50	0.15	Y
	20090905-23	3138 F1 Area-2 UW-Px-4	Fas	1.55	0.08	0.70	0.04	6.48	0.15	Y
	20090905-24	3138 F1 Area-1 UW-Px-1	Fas	1.37	0.07	0.56	0.05	6.48	0.15	Y
	20090905-25	3138 F2 Area-1 UW-Px-1	Fas	2.74	0.14	1.10	0.05	6.23	0.15	Y
	20090905-26	3138 F2 Area-1 UW-Px-2	Fas	1.78	0.09	0.75	0.05	6.14	0.15	Y
	20090905-27	3138 F2 Area-9 UW-Px-1	Fas	2.37	0.12	0.96	0.06	6.10	0.15	Y
	20090905-28	3138 F2 Area-5 UW-Px-1	Fas	2.14	0.11	0.90	0.05	5.98	0.15	Y
	20090908-9	3138 F2 Area-2, Sp-1, in Pyx	Sp	2.58	0.03	1.04	0.04	6.91	0.14	Y
	20090908-10	3138 F2 Area-2, Sp-2, in Pyx	Sp	2.58	0.03	0.99	0.04	6.87	0.14	Y
	20090908-11	3138 F2 Area-4, Sp-1, in Mel	Sp	2.67	0.03	1.03	0.04	2.16	0.14	Y
	20090908-12	3138 F1 Area-2, Sp-3, in Pyx	Sp	2.62	0.03	1.09	0.04	7.64	0.14	Y
	20090908-13	3138 F1 Area-2, Sp-4, in Pyx, crack	Sp	2.49	0.02	0.96	0.04	7.70	0.14	Y
	20090908-14	3138 F1 Area-1, Sp-1, in Pyx	Sp	2.56	0.03	0.97	0.04	7.06	0.14	Y
	20090908-15	3138 F1 Area-1, Sp-2, in Mel	Sp	2.66	0.03	0.96	0.04	3.16	0.14	Y
	20090908-16	3138 F1 Area-6, Sp-1, in An	Sp	2.64	0.03	1.85	0.04	6.60	0.14	
	20090908-17	3137 F1 Area-2, Sp-6, in An	Sp	2.57	0.03	1.20	0.04	7.05	0.14	
	20090908-18	3138 F1 Area-2, Sp-6, in An	Sp	2.94	0.03	2.61	0.04	7.28	0.14	

(continued on next page)

### Author contributions

All coauthors participated in the writing and interpretation. G.J.M. was primarily responsible for writing and interpretation. N.T.K. and T.U. had primary responsibility for isotopic data collection. E.S.B. had primary responsibility for sample characterization, including all SEM imaging and CAI bulk composition plus all electron microprobe mineral analyses. A.M.D. wrote the section and carried out the calculations on magnesium isotopic evolution.

### Acknowledgments

We are grateful to F. Richter for numerous discussions, and to two anonymous reviewers whose detailed and constructive reviews greatly improved the manuscript. This research was supported by NASA grants NNX07AJ05G (G.J.M., PI), NNX09AG39G (A.M.D., PI), and NNX09AB88G (NK, PI). WiscSIMS is partly supported by NSF (EAR03-19230, EAR07-44079).

Table A1 (continued)

CAI name	Analyses #	Analyses spot	Phase analysis (*1)	$^{27}\text{Al}/^{24}\text{Mg}$	$2\sigma$	$\delta^{26}\text{Mg}^*$ (‰)	$2\sigma$ (‰)	$\delta^{25}\text{Mg}$ (‰)	$2\sigma$ (‰)	Isochron fit (*2)
3138 F4	20090908-39	3138 F2 Area-2, Sp-1, in An	Sp	3.06	0.03	1.93	0.05	7.03	0.13	
	20090908-40	3138 F2 Area-2, Sp-2, in An	Sp	3.03	0.03	1.98	0.05	7.15	0.13	
	20090908-41	3138 F2 Area-2, Sp-3, in An	Sp	3.23	0.03	1.77	0.05	7.90	0.13	
	20090908-42	3138 F2 Area-6, Sp-1, in An, crack	Sp	2.69	0.03	1.48	0.05	6.70	0.13	
	20090903-39	3138 F4 Area-1 UW-Mel-5	Mel	11.61	0.09	3.88	0.14	2.89	0.20	A
	20090903-41	3138 F4 Area-1 UW-Mel-7	Mel	12.69	0.10	4.68	0.17	2.72	0.20	A
	20090903-43	3138 F4 Area-1 UW-Mel-9	Mel	16.08	0.13	5.76	0.16	2.71	0.20	A
	20090903-44	3138 F4 Area-1 UW-Mel-10	Mel	14.63	0.11	5.46	0.18	4.88	0.20	A
	20090903-45	3138 F4 Area-1 UW-Mel-11	Mel	12.22	0.10	4.29	0.12	3.28	0.20	A
	20090903-47	3138 F4 Area-1 UW-Mel-13	Mel	13.42	0.11	4.84	0.15	3.38	0.20	A
	20090903-53	3138 F4 Area-4 UW-Mel-3	Mel	12.78	0.10	4.36	0.21	2.84	0.19	A
	20090903-54	3138 F4 Area-4 UW-Mel-4	Mel	10.36	0.08	3.95	0.12	6.84	0.19	A
	20090903-55	3138 F4 Area-4 UW-Mel-5	Mel	17.78	0.14	6.39	0.16	3.57	0.19	A
	20090907-16	3138 F4 Area-1 UW-Px-7	Fas	1.79	0.09	0.62	0.10	2.32	0.37	A
	20090907-19	3138 F4 Area-4 UW-Px-1	Fas	2.78	0.14	1.63	0.09	3.55	0.37	A
	20090907-20	3138 F4 Area-4 UW-Px-2	Fas	1.91	0.10	0.98	0.08	2.58	0.37	A
	20090909-15	3138 F4 Area-4 UW-Sp-2	Sp	2.60	0.03	1.06	0.05	3.85	0.10	A
	20090909-17	3138 F4 Area-1 UW-Sp-4	Sp	2.58	0.03	1.10	0.05	4.21	0.10	A
	20090903-22	3138 F4 Area-3 UW-Mel-4	Mel	2.97	0.02	1.03	0.07	1.97	0.10	C
	20090903-23	3138 F4 Area-3 UW-Mel-5	Mel	3.49	0.03	1.22	0.09	2.19	0.10	C
	20090903-24	3138 F4 Area-7 UW-Mel-1	Mel	3.62	0.03	1.20	0.07	2.35	0.10	C
	20090903-25	3138 F4 Area-7 UW-Mel-2	Mel	2.03	0.02	0.93	0.07	2.04	0.10	C
	20090903-26	3138 F4 Area-7 UW-Mel-3	Mel	3.64	0.03	1.14	0.09	2.35	0.10	C
	20090903-27	3138 F4 Area-7 UW-Mel-4	Mel	1.18	0.01	1.00	0.07	1.87	0.10	C
	20090903-28	3138 F4 Area-6 UW-Mel-1	Mel	0.80	0.01	0.83	0.07	1.43	0.10	C
	20090903-31	3138 F4 Area-6 UW-Mel-4	Mel	1.77	0.01	1.07	0.07	1.79	0.10	C
	20090903-36	3138 F4 Area-5 UW-Mel-2	Mel	0.89	0.01	0.75	0.06	1.28	0.20	C
	20090903-38	3138 F4 Area-2 UW-Mel-1	Mel	0.808	0.006	0.69	0.06	1.39	0.20	C
	20090903-40	3138 F4 Area-1 UW-Mel-6	Mel	2.12	0.02	0.96	0.07	2.70	0.20	C
	20090903-42	3138 F4 Area-1 UW-Mel-8	Mel	2.56	0.02	1.10	0.07	2.62	0.20	C
	20090903-46	3138 F4 Area-1 UW-Mel-12	Mel	2.36	0.02	0.94	0.07	2.74	0.20	C
	20090903-52	3138 F4 Area-1 UW-Mel-14	Mel	2.54	0.02	1.03	0.08	2.56	0.19	C
	20090905-48	3138 F4 Area-11 UW-Px-2	Fas	1.42	0.07	0.75	0.04	1.86	0.21	C
	20090905-49	3138 F4 Area-11 UW-Px-3	Fas	0.97	0.05	0.72	0.05	1.80	0.21	C
	20090905-51	3138 F4 Area-10 UW-Px-1	Fas	1.58	0.08	0.72	0.05	1.69	0.21	C
	20090905-54	3138 F4 Area-1 UW-Px-6	Fas	1.83	0.10	0.81	0.04	2.39	0.21	C
	20090907-21	3138 F4 Area-4 UW-Px-3	Fas	2.02	0.11	0.83	0.05	2.73	0.37	C
	20090907-22	3138 F4 Area-4 UW-Px-4	Fas	1.79	0.09	0.67	0.09	2.24	0.37	C
	20090907-23	3138 F4 Area-4 UW-Px-5	Fas	2.37	0.12	0.92	0.08	2.30	0.37	C
	20090909-22	3138 F4 Area-1 UW-Sp-5	Sp	2.58	0.03	1.02	0.06	3.42	0.08	C
20090909-23	3138 F4 Area-1 UW-Sp-6	Sp	2.57	0.03	1.06	0.06	3.58	0.08	C	
20090909-24	3138 F4 Area-1 UW-Sp-7	Sp	2.58	0.03	1.05	0.06	3.14	0.08	C	
3138 F5	20090415-03&04	3138 F5 AOA-CAI-Mel-1	Mel-EM	22.18	0.39	8.5	1.5	-0.9	1.3	Y
	20090415-05	3138 F5 AOA-CAI-Mel-2	Mel-EM	24.21	0.42	9.7	1.5	-0.6	1.3	Y
	20090415-06	3138 F5 AOA-CAI-Mel-3	Mel-EM	32.15	0.86	13.2	2.6	-1.3	1.8	Y
	20090415-07	3138 F5 AOA-CAI-Mel-4	Mel-EM	27.11	0.47	10.2	1.3	-0.7	1.2	Y
	20090415-08	3138 F5 AOA-CAI-Mel-5	Mel-EM	15.77	0.28	5.1	1.3	-0.2	1.3	Y
	20090909-44	3138 F5 Area-3, Ol-2	Fo	0.011	0.001	-0.006	0.034	-2.82	0.18	Y
	20090909-45	3138 F5 Area-3, Ol-3	Fo	0.011	0.001	-0.002	0.034	-2.68	0.18	Y
	20090909-46	3138 F5 Area-3, Ol-4	Fo	0.026	0.003	-0.031	0.034	-2.65	0.18	Y
	20090909-48	3138 F5 Area-10, Ol-1	Fo	0.033	0.003	-0.019	0.034	-2.72	0.18	Y
	20090909-49	3138 F5 Area-3, Ol-5	Fo	0.0044	0.0004	-0.001	0.034	-2.68	0.18	Y
	20090908-25	3138 F5 Area-8, Sp-1	Sp	2.65	0.03	0.98	0.03	0.81	0.10	Y
	20090908-26	3138 F5 Area-2, Sp-1	Sp	2.61	0.03	0.92	0.03	0.84	0.10	Y
	20090908-27	3138 F5 Area-1, Sp-1	Sp	2.74	0.03	1.00	0.03	0.61	0.10	Y
	20090908-28	3138 F5 Area-1, Sp-2	Sp	2.87	0.03	1.03	0.03	0.55	0.10	Y
	20090908-29	3138 F5 Area-9, Sp-1	Sp	2.60	0.03	0.92	0.03	1.17	0.10	Y
	3138 F6	20090902-40	3138 F6 Area-9 UW-Mel-1	Mel	6.13	0.05	1.78	0.10	1.83	0.38
20090902-41		3138 F6 Area-9 UW-Mel-2	Mel	5.62	0.04	1.70	0.10	2.18	0.38	Y
20090902-42		3138 F6 Area-1 UW-Mel-3	Mel	7.52	0.06	2.57	0.12	3.59	0.38	Y
20090902-43		3138 F6 Area-4 UW-Mel-1	Mel	7.17	0.06	2.30	0.10	3.77	0.38	Y
20090902-44		3138 F6 Area-3 UW-Mel-6	Mel	8.27	0.06	2.61	0.13	1.29	0.38	Y
20090902-45		3138 F6 Area-3 UW-Mel-7	Mel	8.86	0.07	2.81	0.14	1.29	0.38	Y
20090902-46		3138 F6 Area-10 UW-Mel-1	Mel	5.40	0.04	1.67	0.11	2.50	0.38	Y
20090902-47		3138 F6 Area-10 UW-Mel-2	Mel	5.50	0.04	1.82	0.10	2.50	0.38	Y
20090902-48		3138 F6 Area-5 UW-Mel-1	Mel	9.75	0.08	2.93	0.12	1.49	0.38	Y
20090902-49		3138 F6 Area-5 UW-Mel-2	Mel	8.81	0.07	2.87	0.13	0.77	0.38	Y
20090905-33		3138 F6 Area-5 UW-Px-2	Fas	4.49	0.23	1.46	0.05	5.83	0.17	Y
20090905-34		3138 F6 Area-5 UW-Px-3	Fas	3.88	0.20	1.30	0.06	5.99	0.17	Y
20090905-35		3138 F6 Area-11 UW-Px-1	Fas	4.65	0.24	1.43	0.06	2.66	0.17	Y
20090908-23		3138 F6 Area-1, Sp-2	Sp	2.64	0.03	0.96	0.03	4.83	0.10	Y
20090908-24		3138 F6 Area-1, Sp-3	Sp	2.62	0.03	0.99	0.03	4.74	0.10	Y
3138 F8		20090416-08	3138 F8 area 2, Hib-1	Hib-EM	15.2	1.5	6.3	1.2		
	20090416-02	3138 F8 area 1, Mel-1	Mel-EM	15.9	0.3	7.3	1.2	1.0	1.2	Y
	20090416-03	3138 F8 area 1, Mel-2	Mel-EM	16.3	0.3	6.1	1.5	1.8	1.3	Y
	20090416-05	3138 F8 area 1, Mel-4	Mel-EM	18.2	0.3	8.2	1.2	1.1	1.2	Y

Table A1 (continued)

CAI name	Analyses #	Analyses spot	Phase analysis (*1)	$^{27}\text{Al}/^{24}\text{Mg}$	$2\sigma$	$\delta^{26}\text{Mg}^*$ (‰)	$2\sigma$ (‰)	$\delta^{25}\text{Mg}$ (‰)	$2\sigma$ (‰)	Isochron fit (*2)
	20090416-06	3138 F8 area 1, Mel-5, rim	Mel-EM	21.2	0.4	8.1	1.5	-0.5	1.2	Y
	20090416-07	3138 F8 area 2, Mel-1	Mel-EM	86.6	1.6	30.7	2.6	-1.7	1.7	Y
	20090416-09	3138 F8 area 2, Mel-2	Mel-EM	85.6	1.5	32.2	2.8	-1.9	1.8	Y
	20090416-10	3138 F8 area 2, Mel-3	Mel-EM	95.5	1.6	33.6	2.9	-0.7	1.8	Y
	20090416-11	3138 F8 area 2, Mel-4	Mel-EM	91.1	1.7	36.3	3.2	0.1	1.9	Y
	20090416-12	3138 F8 area 2, Mel-5	Mel-EM	44.2	0.8	15.6	2.4	-1.8	1.5	Y
	20090416-13	3138 F8 area 2, Mel-6	Mel-EM	76.6	1.5	28.8	3.5	-2.5	2.0	Y
	20090907-30	3138 F8 Area-3 UW-Px-2	Fas-s	5.10	0.27	2.00	0.12	3.74	0.36	Y
	20090907-31	3138 F8 Area-3 UW-Px-3	Fas-s	4.52	0.24	1.75	0.16	4.53	0.36	Y
	20090907-32	3138 F8 Area-3 UW-Px-4	Fas-s	4.41	0.23	1.58	0.14	2.62	0.36	Y
	20090910-8	3138 F8 Area-2, Sp-2	Sp-s	2.74	0.03	0.81	0.13	-1.34	0.12	Y
	20090910-9	3138 F8 Area-8, Sp-2	Sp-s	2.72	0.03	1.00	0.13	-1.14	0.12	Y
3138 F9	20090910-10	3138 F8 Area-8, Sp-3	Sp-s	2.66	0.03	0.94	0.13	-1.59	0.12	Y
	20090910-11	3138 F8 Area-8, Sp-4	Sp-s	2.66	0.03	0.93	0.13	-1.50	0.12	Y
	20090903-10	3138 F9 Area-1 UW-Mel-2	Mel	8.43	0.07	3.00	0.11	8.27	0.17	Y
	20090903-11	3138 F9 Area-1 UW-Mel-3	Mel	7.27	0.06	2.52	0.10	8.25	0.17	Y
	20090903-12	3138 F9 Area-5 UW-Mel-1	Mel	11.74	0.09	4.59	0.16	4.10	0.17	Y
	20090903-13	3138 F9 Area-5 UW-Mel-2	Mel	9.77	0.08	3.77	0.10	8.82	0.17	Y
	20090903-14	3138 F9 Area-6 UW-Mel-1	Mel	6.96	0.05	2.56	0.11	8.33	0.17	Y
	20090903-15	3138 F9 Area-6 UW-Mel-2	Mel	7.18	0.06	2.62	0.13	8.38	0.17	Y
	20090903-7	3138 F9 Area-3 UW-Mel-1	Mel	9.09	0.07	3.20	0.11	9.57	0.17	Y
	20090903-8	3138 F9 Area-3 UW-Mel-2	Mel	7.67	0.06	2.75	0.11	8.23	0.17	Y
	20090903-9	3138 F9 Area-1 UW-Mel-1	Mel	7.94	0.06	2.97	0.12	8.20	0.17	Y
	20090905-36	3138 F9 Area-3 UW-Px-1	Fas	3.62	0.19	1.37	0.07	8.27	0.17	Y
	20090905-37	3138 F9 Area-3 UW-Px-2	Fas	3.34	0.17	1.28	0.06	8.17	0.17	Y
	20090905-38	3138 F9 Area-3 UW-Px-3	Fas	4.09	0.21	1.63	0.06	8.24	0.17	Y
	20090908-35	3138 F9 Area-5, Sp-1	Sp	2.77	0.03	1.06	0.05	9.77	0.13	Y
	20090908-36	3138 F9 Area-1, Sp-1	Sp	2.59	0.03	1.06	0.05	9.07	0.13	Y
	20090908-37	3138 F9 Area-2, Sp-1	Sp	2.58	0.03	0.96	0.05	9.40	0.13	Y
	20090908-38	3138 F9 Area-6, Sp-1	Sp	2.60	0.03	0.95	0.05	9.26	0.13	Y

(\*1) Default beam size and intensity.

Mel, Fas 25  $\mu\text{m}$  plus aberration, 20 nA  
 Fas-s 25  $\mu\text{m}$ , 7 nA  
 Sp, Fo 25  $\mu\text{m}$ , 7 nA  
 Sp-s 10  $\mu\text{m}$ , 3 nA  
 Mel-EM 4  $\times$  6  $\mu\text{m}$ , 70 pA  
 An 4  $\times$  6  $\mu\text{m}$ , 140 pA

(\*2) "Y" indicates data used for isochron regression, except for F4. "A" and "C" for F4 indicate data used for isochron regressions of Type A island and Type C mantle areas of the inclusion, respectively.

(\*3) Sample "F2" is another section of CAI "F1".

## References

- Amelin, Y., Krot, A.N., Hutcheon, I.D., Ulyanov, A.A., 2002. Lead isotopic ages of chondrules and calcium–aluminum-rich inclusions. *Science* 297, 1678–1683.
- Bouvier, A., Wadhwa, M., 2010. The age of the solar system redefined by the oldest Pb–Pb age of a meteoritic inclusion. *Nature Geosci.* 3, 637–641.
- Bullock, E.S., MacPherson, G.J., 2008. Creating a new, comprehensive CAI reference suite, part one: Vigarano. *Meteorit. Planet. Sci.* 43, A29.
- Bullock, E.S., MacPherson, G.J., Krot, A.N., 2007. Forsterite-bearing type B CAIs: bulk composition evidence for a hybrid origin. *Meteorit. Planet. Sci.* 42, A26.
- Davis, A.M., Richter, F.M., Mendybaev, R.A., Janney, P.E., Wadhwa, M., McKeegan, K.D., 2005. Isotopic mass fractionation laws and the initial solar system  $^{26}\text{Al}/^{27}\text{Al}$  Ratio. *Lunar Planet. Sci.* 36 (abstract #2334).
- Gray, C.M., Papanastassiou, D.A., Wasserburg, G.J., 1973. The identification of early condensates from the solar nebula. *Icarus* 20, 213–239.
- Hsu, W., Wasserburg, G.J., Huss, G.R., 2000. High time resolution by use of the  $^{26}\text{Al}$  chronometer in the multistage formation of a CAI. *Earth Planet. Sci. Lett.* 182, 15–29.
- Ito, M., Ganguly, J., 2009. Mg diffusion in minerals in CAIs: new experimental data for melilites and implications for the Al–Mg chronometer and thermal history of CAIs. *Lunar Planet. Sci.* XL A1753.
- Jacobsen, B., Yin, Q.-Z., Moynier, F., Amelin, Y., Krot, A.N., Nagashima, K., Hutcheon, I.D., Palme, H., 2008.  $^{26}\text{Al}/^{27}\text{Al}$  and  $^{207}\text{Pb}/^{206}\text{Pb}$  systematics of Allende CAIs: canonical solar initial  $^{26}\text{Al}/^{27}\text{Al}$  ratio reinstated. *Earth Planet. Sci. Lett.* 272, 353–364.
- Kita, N.T., Ushikubo, T., in press. Evolution of protoplanetary disk inferred from  $^{26}\text{Al}$  chronology of individual chondrules. *Meteorit. Planet. Sci.* doi:10.1111/j.1945-5100.2011.01264.x.
- Kita, N.T., Ushikubo, T., Knight, K.B., Mendybaev, R.A., Davis, A.M., Richter, F.M., Fournelle, J.H., in press. Internal  $^{26}\text{Al}$ – $^{26}\text{Mg}$  isotope systematics of a Type B CAI: Remelting of refractory precursor solids. *Geochim. Cosmochim. Acta.* doi:10.1016/j.gca.2012.02.015.
- Larsen, K.K., Trinquier, A., Paton, C., Schiller, M., Wielandt, D., Ivanova, M.A., Connelly, J.N., Nordlund, Å., Krot, A.N., Bizzarro, M., 2011. Evidence for magnesium isotope heterogeneity in the solar protoplanetary disk. *Astrophys. J. Lett.* 735, L37–L45.
- Liermann, H.-P., Ganguly, J., 2002. Diffusion kinetics of  $\text{Fe}^{2+}$  and Mg in aluminous spinel: experimental determination and applications. *Geochim. Cosmochim. Acta* 66, 2903–2913.
- Lodders, K., Palme, H., Gail, H.-P., 2009. Abundances of the elements in the solar system. *Landolt–Börnstein—Group VI Astronomy and Astrophysics, Volume 4B: Solar System*. Springer-Verlag, Berlin. doi:10.1007/978-3-540-88055-4\_34.
- MacPherson, G.J., 2007. Calcium–aluminum-rich inclusions in chondritic meteorites. In: Davis, A.M. (Ed.), *Meteorites, Planets, and Comets*, 2nd ed.: In: Holland, H.D., Turekian, K.K. (Eds.), *Treatise on Geochemistry*, vol. 1. Elsevier, Oxford. published electronically at <http://www.sciencedirect.com/science/referenceworks/9780080437514>.
- MacPherson, G.J., Davis, A.M., Zinner, E.K., 1995. The distribution of aluminum-26 in the early solar system—a reappraisal. *Meteoritics* 30, 365–386.
- MacPherson, G.J., Bullock, E.S., Janney, P.E., Kita, N.T., Ushikubo, T., Davis, A.M., Wadhwa, M., Krot, A.N., 2010. Early solar nebula condensates with canonical, not supracanonical, initial  $^{26}\text{Al}/^{27}\text{Al}$  ratios. *Astrophys. J. Lett.* 711, L117–L121.
- Norris, T.L., Gancarz, A.J., Rokop, D.J., Thomas, K.W., 1983. Half-life of  $^{26}\text{Al}$ . *J. Geophys. Res.* 88 (S1), B331–B333.
- Podosek, F.A., Zinner, E.K., MacPherson, G.J., Lundberg, L., Brannon, J.C., Fahey, A.J., 1991. Correlated study of initial  $^{87}\text{Sr}/^{86}\text{Sr}$  and Al–Mg isotopic systematics and petrologic properties in a suite of refractory inclusions from the Allende meteorite. *Geochim. Cosmochim. Acta* 55, 1083–1110.
- Richter, F.M., Davis, A.M., Ebel, D.S., Hashimoto, A., 2002. Elemental and isotopic fractionation of type B CAIs: experiments, theoretical considerations, and constraints on their thermal history. *Geochim. Cosmochim. Acta* 66, 521–540.
- Richter, F.M., Mendybaev, R.A., Davis, A.M., 2006. Conditions in the protoplanetary disk as seen by refractory inclusions in meteorites. *Meteorit. Planet. Sci.* 41, 83–93.

- Sheng, Y.J., Hutcheon, I.D., Wasserburg, G.J., 1992. Self-diffusion of magnesium in spinel and in equilibrium melts: constraints on flash heating of silicates. *Geochim. Cosmochim. Acta* 56, 2535–2546.
- Thrane, K., Bizzarro, M., Baker, J.A., 2006. Extremely brief formation interval for refractory inclusions and uniform distribution of  $^{26}\text{Al}$  in the early solar system. *Astrophys. J.* 646, L159–L162.
- Villeneuve, J., Chaussidon, M., Libourel, G., 2009. Homogeneous distribution of  $^{26}\text{Al}$  in the solar system from the Mg isotopic composition of chondrules. *Science* 325, 985–988.
- Young, E.D., Simon, J.I., Galy, A., Russell, S.S., Tonui, E., Lovera, O., 2005. Supra-canonical  $^{26}\text{Al}/^{27}\text{Al}$  and the residence time of CAIs in the solar protoplanetary disk. *Science* 308, 223–227.